Palmer-Chalker correlations in the XY pyrochlore antiferromagnet $Er_2Sn_2O_7$

Solene Guitteny,[1] Sylvain Petit,[1] Elsa Lhotel,[2] Julien Robert,[1] Pierre Bonville,[3] Anne Forget,[3] and Isabelle Mirebeau[1]
[1]*CEA, Centre de Saclay, DSM/IRAMIS/Laboratoire Léon Brillouin, F-91191 Gif-sur-Yvette, France*
[2]*Institut Néel, CNRS, 25 Av des martyrs, BP 25, 38042 Grenoble Cedex, France*
[3]*CEA, Centre de Saclay, DSM/IRAMIS/Service de Physique de l'Etat Condensé, F-91191 Gif-Sur-Yvette, France*
(Received 24 April 2013; revised manuscript received 30 August 2013; published 10 October 2013)

$Er_2Sn_2O_7$ is considered, together with $Er_2Ti_2O_7$, as a realization of the XY antiferromagnet on the pyrochlore lattice. We present magnetization measurements confirming that $Er_2Sn_2O_7$ does not order down to 100 mK but exhibits a freezing below 200 mK. Our neutron scattering experiments evidence the strong XY character of the Er^{3+} moment and point out the existence of short-range correlations in which the magnetic moments are in peculiar configurations, the Palmer-Chalker states, predicted theoretically for an XY pyrochlore antiferromagnet with dipolar interactions. Our estimation of the $Er_2Sn_2O_7$ parameters confirm the role of the latter interactions on top of relatively weak and isotropic exchange couplings.

DOI: 10.1103/PhysRevB.88.134408 PACS number(s): 75.25.−j, 61.05.F−, 75.40.−s, 75.50.Ee

I. INTRODUCTION

Geometrical frustration has become a central challenge in contemporary condensed matter physics. It is the source of many exotic ground states whose description remains challenging for both theoreticians and experimentalists.[1] These unconventional magnetic states often originate from the strong degeneracy of the ground state manifold, which prevents the stabilization of standard magnetic phases. Whatever their type, perturbations are often driving the low-temperature behaviors by lifting partially or totally this extensive degeneracy. Quantum or thermal fluctuations may also enter into play to select and stabilize a particular configuration (or a subset of configurations), a phenomenon called "order by disorder" mechanism.[2] The family of pyrochlore compounds $R_2T_2O_7$ (R is a rare earth and T = Ti, Sn, Zr,...), with the rare-earth magnetic moments localized at the vertices of corner-sharing tetrahedra are model systems to study these subtle order by disorder effects.[3,4]

The case of R = Er compounds is of specific interest: They present a strong XY-like anisotropy, combined with antiferromagnetic interactions leading to a model with an extensive classical degeneracy.[5,6] The easy magnetic planes are perpendicular to the local ⟨111⟩ ternary axes (XY character), arising from the crystal field properties of the Kramers Er^{3+} ion. While no signature of long-range order could be detected down to 100 mK in $Er_2Sn_2O_7$,[7–9] $Er_2Ti_2O_7$ undergoes a transition towards an antiferromagnetic Néel phase below $T_N = 1.2$ K.[10–12] This ordered phase has a noncollinear structure, in which the magnetic moments are perpendicular to the local ⟨111⟩ axes in a peculiar configuration denoted ψ_2.[13,14] In $Er_2Ti_2O_7$, this structure is surprising since dipolar interactions, which are an important perturbation to the isotropic exchange Hamiltonian, are expected to select other magnetic states, called Palmer-Chalker states.[13,15] However, by considering general anisotropic exchange parameters, it has been recently argued that a quantum order by disorder mechanism[16–18] explains this ψ_2 ordering and accounts for many experimental features. In this context, the reasons for the absence of ordering in $Er_2Sn_2O_7$ remain an open question.

In this paper we address this issue by determining experimentally the key parameters of the Hamiltonian of $Er_2Sn_2O_7$: The crystal electric field (CEF) parameters obtained from inelastic neutron scattering experiments and the anisotropic exchange parameters deduced from the magnetization curves. The main difference between the titanate and stannate parameters is a weaker and less anisotropic exchange tensor. By analyzing neutron scattering data, we demonstrate the existence of short-range correlated domains frozen in the Palmer-Chalker configurations,[15] hence quite different from the ψ_2 configuration selected in $Er_2Ti_2O_7$.[13,14] We finally show that these configurations are indeed stabilized in a mean-field calculation for this set of parameters.

Magnetization and ac susceptibility measurements were performed on a powder sample down to 100 mK using a superconducting quantum interference device (SQUID) magnetometer equipped with a dilution refrigerator developed at the Institut Néel-CNRS Grenoble.[19] The neutron measurements were performed on the same sample at the cold triple-axis spectrometer 4F2 of LLB-Orphée reactor.[20]

II. MAGNETIZATION AND SUSCEPTIBILITY

Our magnetization measurements first confirm the absence of transition towards a long-range ordered state down to 100 mK. The dc susceptibility keeps increasing with decreasing temperature. It presents an upturn below about 2 K, hence deviating from a Curie-Weiss behavior (see the top inset of Fig. 1), in agreement with Ref. 7. Below 200 mK, a freezing is observed, as shown by an irreversibility in the zero-field-cooled–field-cooled (ZFC-FC) magnetization and by a frequency dependence in the ac susceptibility (see top of Fig. 1). The imaginary part of the susceptibility χ'' exhibits a peak whose frequency dependence can be accounted for by an Arrhenius law $\tau = \tau_0 \exp(E/k_BT)$, where $\tau = 1/2\pi f$, $\tau_0 = 4 \times 10^{-5}$ s, and $E/k_B = 0.9$ K (see bottom of Fig. 1) in the measured frequency range (0.57–211 Hz). Qualitatively similar features have been observed in this temperature range in other spin-liquid compounds such as $Gd_3Ga_5O_{12}$[21] or $Tb_2Ti_2O_7$.[22–24] At the moment, no clear picture emerges to explain this freezing, but it could be associated with slow dynamics of correlated spins.

The magnetization curves as a function of field present an inflection point around 1 T for temperatures below 750 mK

 ©2013 American Physical Society

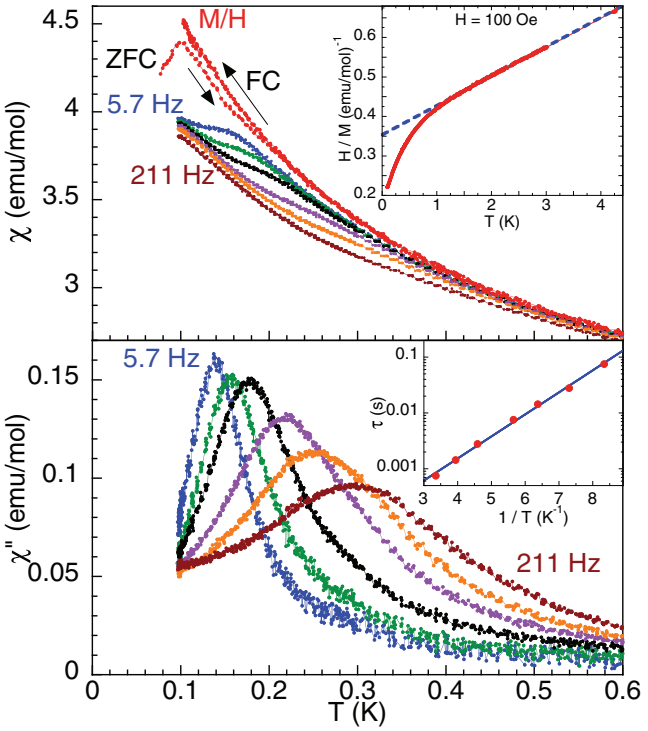

FIG. 1. (Color online) ac and dc susceptibility vs temperature. ac susceptibility is plotted for $5.7 < f < 211$ Hz with $H_{ac} = 1.4$ Oe. Top: M/H and real part of the ac susceptibility χ' vs T. M was measured using the ZFC-FC procedure with $H = 50$ Oe. Inset: H/M vs T for $H = 100$ Oe. The dotted line is a fit to the equation $H/M = 0.35 + 0.07T$. Bottom: χ'' vs T. Inset: τ vs $1/T_{max}$ showing the Arrhenius behavior with $\tau_0 = 4 \times 10^{-5}$ s and $E/k_B = 0.9$ K.

(see Fig. 2). This behavior is reminiscent of the field induced transition observed in $Er_2Ti_2O_7$,[25–28] thus suggesting that a field induced order might be stabilized above this field in $Er_2Sn_2O_7$. Unfortunately, the powder nature of the sample prevents us from a detailed analysis of this metamagneticlike behavior. However, it is worth mentioning that preliminary calculations (using the mean-field model developed in Sec. V) indicate that reorientations of the magnetic moments occur in the 1–1.5 T field range for the three main symmetry directions [110], [100], and [111].

Below 200 mK, an additional curvature develops in the magnetization curve around 0.2 T (see inset of Fig. 2) which might be associated with the freezing observed in low field at these temperatures.

III. *XY* ANISOTROPY AND CRYSTAL FIELD ANALYSIS

Aiming at a precise determination of the Er^{3+} anisotropy, the CEF excitations were measured by means of inelastic neutron scattering experiments (see Fig. 3), carried out at temperatures of 1.5, 10, 50, and 100 K. Between 0 and 20 meV, three CEF levels are observed at $E_1 = 5.1$, $E_2 = 7.6$, and $E_3 = 17.2$ meV, in agreement with Ref. 8. With increasing temperature, excited states are populated to the detriment of the ground CEF state, giving rise to new modes at $\hbar\omega = E_i - E_j$. The analysis of these spectra is based on the simulation of the

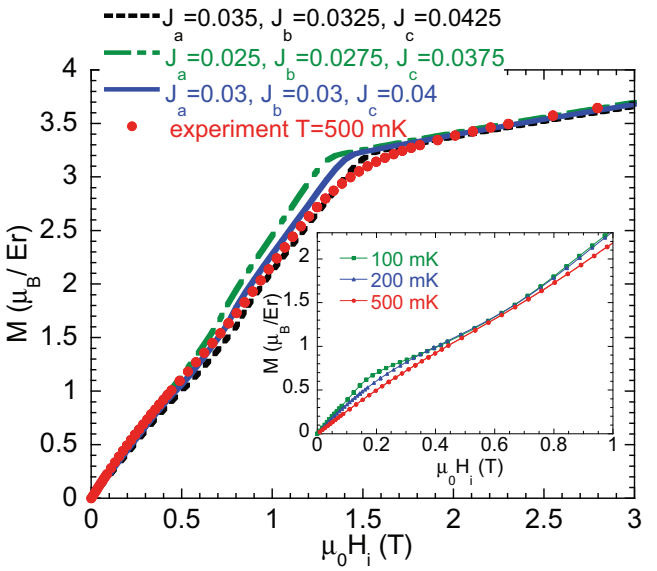

FIG. 2. (Color online) Magnetization M vs internal field H_i (points), along with simulation (lines) (see text). Corrections for demagnetizing effects were made assuming a demagnetizing factor $N = 4\pi/3$ (cgs units).[33] Results for different sets of parameters (assuming $J_4 = 0$) are presented to illustrate the sensitivity of the calculation. Inset: M vs H_i for $\mu_0 H_i < 1$ T at 100 (green squares), 200 (blue triangles), and 500 mK (red points).

scattering function $S(Q,\omega)$:

$$S(Q,\omega) = \sum_{m,n} \frac{e^{-E_m/k_BT}}{Z} \langle m|\vec{J}|n\rangle\langle n|\vec{J}|m\rangle \times \delta(\omega + E_n - E_m),$$

where the $|m\rangle$ and E_m are, respectively, the eigenwave functions and eigenvalues of the CEF Hamiltonian $\mathcal{H}_{CEF}$

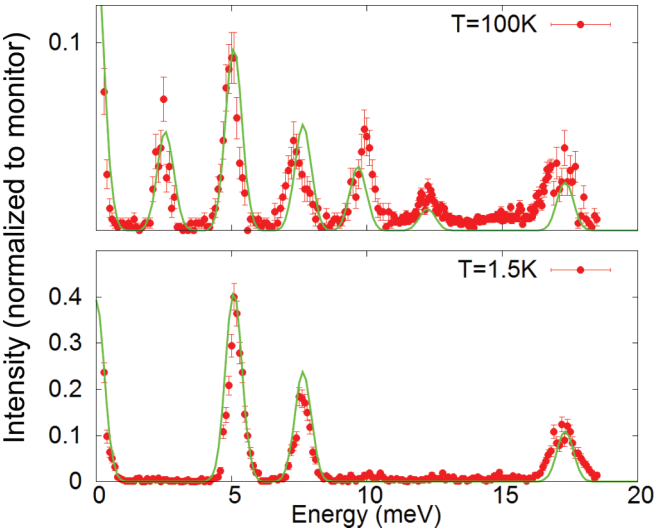

FIG. 3. (Color online) Inelastic neutron scattering spectra showing the CEF excitations. The lines correspond to the calculation (see text) with the parameters obtained from the fit at 1.5 K. At 100 K, the slight discrepancy is attributed to a small evolution of the parameters with temperature.

TABLE I. Stevens coefficients (in K) for $Er_2Sn_2O_7$ (present work) and $Er_2Ti_2O_7$ (from Ref. 29).

	B_{20}	B_{22}	B_{40}	B_{42}	B_{43}	B_{60}	B_{63}	B_{66}	$g_\perp$	$g_\parallel$
$Er_2Ti_2O_7$	616	0	2850	0	795	858	−493	980	6.8	2.6
$Er_2Sn_2O_7$	656	0	3010	0	755	738	−653	990	7.52	0.054

($J = 15/2$, $g_J = 6/5$ for Er^{3+}):

$$\mathcal{H}_{\rm CEF} = \sum_{m,n} B_{nm} O_{nm}.$$

The O_{nm} are the Stevens operators and the B_{nm} are the associated coefficients that remain to be determined (Ref. 29 and references therein). Z is the partition function defined by $Z = \sum_m e^{-E_m/k_BT}$. Fitting the data through this model yields the coefficients listed in Table I (see also Appendix A). The wave functions of the ground doublet lead to $g_\perp = 7.52 \pm 0.1$ and $g_\parallel = 0.054 \pm 0.02$. For comparison, the $Er_2Ti_2O_7$ values from Ref. 29 are also given, showing that both compounds have rather similar CEF schemes, but that the Er^{3+} magnetic moment has a stronger planar character in $Er_2Sn_2O_7$.

IV. DIFFUSE ELASTIC SCATTERING AND PALMER-CHALKER CORRELATIONS

To further describe the spin liquid state of $Er_2Sn_2O_7$, we have measured the spin-spin correlation function $S(Q,\omega)$ at 1.5 K. An elastic response is observed, forming a broad peak centered at $Q = 1.1$ Å^{-1}, consistent with the results of Ref. 8. This response is typical of an elastic diffuse scattering where spin correlations extend over a few interatomic distances and are frozen at the time scale of the neutron probe. It is accompanied by a quasielastic contribution corresponding to fluctuations of this short-range ordered pattern with typical rate $\gamma = 0.5$ meV, namely a typical time of $\tau \sim 10$ ps. The intensities of both contributions increase continuously with decreasing temperature.

Such a diffuse peak does not preclude any type of magnetic correlations in general. However, given the similarities between $Er_2Sn_2O_7$ and $Er_2Ti_2O_7$, both being antiferromagnets and sharing an XY anisotropy, we propose to model the magnetic ground state in $Er_2Sn_2O_7$ by considering finite size magnetic domains (to account for the peak broadening), chosen among the symmetry allowed patterns for a $\mathbf{k} = 0$ propagation vector. This modeling is based on a refinement which is constrained by symmetry and physical arguments, as explained below.

The symmetry analysis, performed in the space group Fd-$3m$ using the BasIreps software[30] shows that the basis states of the $\mathbf{k} = 0$ manifold transform as linear combinations of the basis vectors of four irreducible representations (IRs), labeled $\Gamma_{3,5,7,9}$ in group theory.[13,14] The XY anisotropy is minimized only for (i) linear combinations of the two basis vectors ψ_1 and ψ_2 which transform according to Γ_5; and (ii) a discrete set of basis vectors $\psi_{3,4,5}$ which transform according to Γ_7.[31] The ground state of $Er_2Ti_2O_7$ and the Palmer-Chalker states (PC)[15] correspond to ψ_2 and $\psi_{3,4,5}$, respectively, namely to different IRs. Table II and the right side of Fig. 4 provide the coordinates of these basis vectors and a sketch of the ψ_2 and ψ_3 magnetic structures (see also Appendix B).

TABLE II. Coordinates of the moments at the four sites of a tetrahedron in the different ψ sets (see text). Note that $\psi_{3,4,5}$ are obtained by reversing a pair of antiparallel spins in the ψ_1 series.

Site		1	2	3	4
CEF axis		(1,1, − 1)	(−1, − 1, − 1)	(−1,1,1)	(1, − 1,1)
Γ_5	ψ_1	(−1,1,0)	(1, − 1,0)	(1,1,0)	(−1, − 1,0)
		(0,1,1)	(0, − 1,1)	(0,1, − 1)	(0, − 1, − 1)
		(1,0,1)	(−1,0,1)	(−1,0, − 1)	(1,0, − 1)
	ψ_2	(1,1,2)	(−1, − 1,2)	(−1,1, − 2)	(1, − 1, − 2)
		(−2,1, − 1)	(2, − 1, − 1)	(2,1,1)	(−2, − 1,1)
		(−1,2,1)	(1, − 2,1)	(1,2, − 1)	(−1, − 2, − 1)
Γ_7	ψ_3	(1, − 1,0)	(−1,1,0)	(1,1,0)	(−1, − 1,0)
	ψ_4	(0,1,1)	(0,1, − 1)	(0, − 1,1)	(0, − 1, − 1)
	ψ_5	(−1,0, − 1)	(−1,0,1)	(1,0,1)	(1,0, − 1)

We proceed by fitting the crystalline structure at 50 K to determine the overall scaling factor and the lattice parameters. Using these values and assuming a given ψ set, the two remaining parameters of the proposed model are the amplitude of the Er^{3+} moment and the coherence length of the magnetic domains, which determines the width of the diffuse peaks. As shown in Fig. 4, subtracting the high temperature data (50 K) to focus on the magnetic signal only, a very good refinement is obtained with the vectors $\psi_{3,4,5}$ of Γ_7, yielding an Er^{3+} moment of 2.8 μ_B at 1.5 K and a coherence length of about 10 Å.[32] A much worse agreement is obtained with the vectors ψ_1 or ψ_2 of Γ_5. In the data ($Q < 1.7$ Å^{-1}) of Ref. 8, the diffuse peak, and so the Er^{3+} moment, keep increasing down to 100 mK. By comparison with the present results, the Er^{3+} moment likely reaches 3.8 μ_B at 100 mK. Note that powder measurements

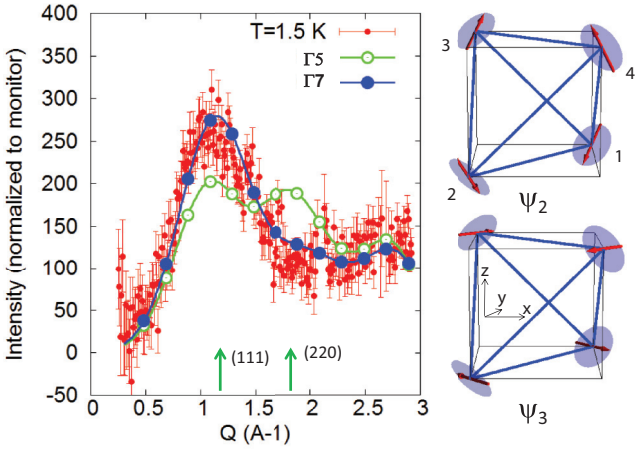

FIG. 4. (Color online) Left: Diffuse magnetic scattering measured by neutron scattering at 1.5 K. "High" temperature reference data ($T = 50$ K) have been subtracted. Exclusion zones have been considered around $Q = 2$ Å^{-1} to eliminate an artifact due to a slight temperature shift of a nuclear peak. The lines are the result of a Rietveld fit assuming either the $\psi_{1,2}$−Γ_5 (green open circles) or the $\psi_{3,4,5}$−Γ_7 (blue solid circles) structure. Right: Magnetic configurations ψ_2 and ψ_3 (see text and Table II) predicted by the symmetry analysis for the $\mathbf{k} = 0$ propagation vector.

cannot distinguish between the basis vectors of either Γ_5 or Γ_7. However, for a given representation, the relative intensities of the (111) and (220) peaks are fixed. The choice between Γ_5 and Γ_7 IRs is thus unambiguous.

V. ESTIMATION OF THE EXCHANGE CONSTANTS IN $Er_2Sn_2O_7$, ANALYSIS AND DISCUSSION

We proceed with the estimation of the exchange constants in $Er_2Sn_2O_7$ by combining neutron data and magnetization curve analyses. As emphasized above, applying a magnetic field drives the system towards an ordered state, hence making a mean-field treatment an acceptable starting point. We thus follow the mean-field approach proposed in Ref. 16, and consider the Heisenberg Hamiltonian for R moments $\vec{J}_i$ at sites i of the pyrochlore lattice:

$$\mathcal{H} = \mathcal{H}_{\rm CEF} + \sum_{\langle i,j \rangle} \vec{J}_i(\tilde{\mathcal{J}} + \tilde{\mathcal{J}}{\rm dip}_{i,j})\langle \vec{J}_j \rangle + g_J \mu_B \vec{H} \cdot \vec{J}_i.$$

In this expression, $\vec{H}$ is an applied magnetic field, $\tilde{\mathcal{J}}$ denotes an (anisotropic) exchange tensor, and $\tilde{\mathcal{J}}{\rm dip}_{i,j}$ is the dipolar interaction limited to the contribution of the nearest neighbors. Various conventions have been used to define this anisotropic exchange.[16–18,34,35] Here we assume an exchange tensor which is diagonal in the $(\vec{a},\vec{b},\vec{c})$ frame linked with a R-R bond:[35]

$$\vec{J}_i \tilde{\mathcal{J}} \vec{J}_j = \sum_{\mu,\nu=x,y,z} J_i^{\mu}\left(\mathcal{J}_a a_{ij}^{\mu} a_{ij}^{\nu} + \mathcal{J}_b b_{ij}^{\mu} b_{ij}^{\nu} + \mathcal{J}_c c_{ij}^{\mu} c_{ij}^{\nu}\right) J_j^{\nu} + \mathcal{J}_4 \sqrt{2} \vec{b}_{ij}(\vec{J}_i \times \vec{J}_j).$$

Considering for instance the pair of Er^{3+} ions at $\vec{r}_1 = (1/4,3/4,0)a$ and $\vec{r}_2 = (0,1/2,0)a$, where a is the cubic lattice constant, we define the local bond frame as $\vec{a}_{12} = (0,0,-1)$, $\vec{b}_{12} = 1/\sqrt{2}(1,-1,0)$, and $\vec{c}_{12} = 1/\sqrt{2}(-1,-1,0)$. This Hamiltonian, written in terms of bond-exchange constants, has the great advantage to provide a direct physical interpretation of the different parameters.

The magnetization is given by $M(\vec{H}) = \sum_i \vec{m}_i \frac{\vec{H}}{H}$, where the $\vec{m}_i$ denote the individual magnetic moments. To carry out this calculation we assume a $\mathbf{k} = 0$ magnetic structure in the Fd-$3m$ space group with face centered cubic (fcc) symmetry. In other words, the four Er^{3+} moments of a given tetrahedron may be different, but the spin configurations on tetrahedra connected by fcc lattice translations are the same. Following a self-consistent treatment, $\mathcal{H}$ is diagonalized numerically for each site to determine the energies $E_{i,\mu}$ and the wave functions $|\psi_{i,\mu}\rangle$. This yields the magnetic moment (see also Appendix C)

$$\vec{m}_i = -g_J \mu_B \langle \vec{J}_i \rangle = -g_J \mu_B \sum_{\mu} \frac{e^{-E_{i,\mu}/k_B T}}{Z} \langle \psi_{i,\mu} | \vec{J}_i | \psi_{i,\mu} \rangle,$$

where $Z = \sum_{\mu} \exp(-E_{i,\mu}/k_B T)$. For a given field amplitude, this procedure is repeated for different directions to account for the powder average.

Since $\mathcal{J}_4$ is an antisymmetric exchange constant (Dzyaloshinskii-Moriya like), it is expected to be smaller than the symmetric ones $\mathcal{J}_{a,b,c}$. Assuming $\mathcal{J}_4 = \pm 0.005$ K,[37] the magnetization curve is then well reproduced by the blue and black sets of parameters in Fig. 2:

$$\mathcal{J}_a \sim 0.03 \pm 0.017 \text{ K}, \quad \mathcal{J}_b \sim 0.03 \pm 0.005 \text{ K}, \quad \mathcal{J}_c \sim 0.04 \pm 0.005 \text{ K}.$$

TABLE III. Anisotropic exchange parameters for $Er_2Sn_2O_7$ (present work) and $Er_2Ti_2O_7$.[17,36] Error bars are given in parentheses. Positive values correspond to antiferromagnetic couplings. The conversion from original values[17] to the $\mathcal{J}_{a,b,c,4}$ set is detailed in Appendix D.

Coupling	$Er_2Sn_2O_7$ (present work)	$Er_2Ti_2O_7$ (Ref. 17)	$Er_2Ti_2O_7$ (Ref. 36)
$\mathcal{J}_a$	0.03 (± 0.017)	−0.078 (± 0.06)	−0.030 (± 0.01)
$\mathcal{J}_b$	0.03 (± 0.005)	0.078 (± 0.01)	0.05 (± 0.005)
$\mathcal{J}_c$	0.04 (± 0.005)	0.078 (± 0.07)	0.105 (± 0.01)
$\mathcal{J}_4$	± 0.005	0.02 (± 0.03)	± 0.005
$g_\perp$	7.52	5.97	6.8
$g_\parallel$	0.054	2.45	2.6

Incorporating the nearest neighbors contribution of the dipolar interaction ($D_{\rm nn} = 0.022$ K, see Appendix C) in these anisotropic exchange constants leads to the effective parameters $\mathcal{J}'_a \sim 0.05 \pm 0.017$ K, $\mathcal{J}'_b \sim 0.05 \pm 0.005$ K, and $\mathcal{J}'_c \sim \pm 0.005$ K.

Next, it is of great interest to compare these results with the $Er_2Ti_2O_7$ exchange parameters listed in Table III and obtained from spin waves[17] or magnetization curve analysis.[36] We first note that the $\mathcal{J}_4$ value in $Er_2Ti_2O_7$ is also almost zero when considering the error bars. Interestingly, the symmetric exchange couplings in $Er_2Sn_2O_7$ are smaller and more isotropic than in $Er_2Ti_2O_7$, thus making the dipolar interaction the main anisotropic interaction.

In this context, according to a number of theoretical works,[6,15,16] the ground states in $Er_2Sn_2O_7$ should belong to the Γ_7 representation, that is to say to the Palmer-Chalker states. The mean-field phase diagram (see Fig. 5) computed in zero field as a function of $\mathcal{J}_a/\mathcal{J}_c$ and $\mathcal{J}_b/\mathcal{J}_c$ confirms this assumption. As quoted in Ref. 16, the energetic selection at play in this approach is quite weak and neglects the influence of quantum and thermal fluctuations. Nonetheless, it is useful to explore the type of correlations that might develop depending on the exchange parameters. First, the calculation predicts a canted ferromagnetic (CF) state in the negative $\mathcal{J}_b/\mathcal{J}_c$ region, which might be relevant in the case of other XY pyrochlores, namely $Yb_2Ti_2O_7$[3,38] or $Yb_2Sn_2O_7$.[39] As for the $Er_2Ti_2O_7$ parameters, they lead in this phase diagram to a long-range ordered antiferromagnetic phase labeled AF1, almost identical to ψ_2 (Γ_5). This ground state is obtained for a strongly anisotropic exchange tensor and especially for ferromagnetic and weakly antiferromagnetic $\mathcal{J}_a/\mathcal{J}_c$. Finally, the $Er_2Sn_2O_7$ parameters lead to a different ground state labeled AF2, which exactly corresponds to the Palmer-Chalker states (Γ_7), with a magnetic moment of 3.9 μ_B and a mean-field ordering temperature $T_N \sim 1.3$ K.

The obtained energy difference between the three states of Γ_7 is very small so that the ultimate selection is expected to be very fragile with respect to any fluctuations. This mean-field phase diagram thus confirms that the anisotropy and exchange parameters in $Er_2Sn_2O_7$ stabilize Palmer-Chalker correlations

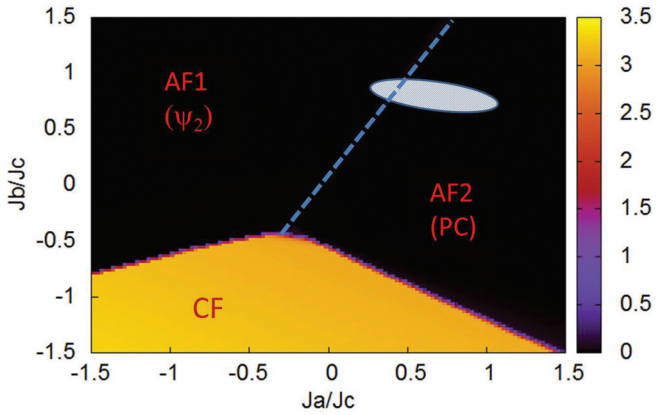

FIG. 5. (Color online) Mean-field phase diagram for $Er_2Sn_2O_7$ (with the above determined CEF coefficients). $\mathcal{J}_c$ and $\mathcal{J}_4$ are fixed to 0.04 K and 0, respectively, while dipolar interaction is included. The AF1 phase resembles very much the ψ_2 state with the moments coordinates at the four sites (x,x,y), $(-x,-x,y)$, $(-x,x,-y)$, and $(x,-x,-y)$ and $y \approx 2x$. The moments coordinates in the CF phase are (x,x,y), $(-x,-x,y)$, $(x,-x,y)$, and $(-x,x,y)$. The shaded area corresponds to the region that accounts for the $M(H)$ measurements at 500 mK in $Er_2Sn_2O_7$.

as measured experimentally, suggesting that $Er_2Sn_2O_7$ is akin to an XY pyrochlore antiferromagnet with dipolar interactions.

The role of the latter interactions in stabilizing Palmer-Chalker states was pointed out in the case of the Heisenberg pyrochlore $Gd_2Sn_2O_7$. It undergoes a first-order transition towards a long-range order at about 1 K,[40–43] this ordering being robust with respect to quantum fluctuations.[44] The lack of ordering in $Er_2Sn_2O_7$ thus remains puzzling, but the XY anisotropy as well as the proximity of the AF1 phase might be key ingredients to explain it.

VI. SUMMARY

In summary, $Er_2Sn_2O_7$ does not exhibit long-range order down to the base temperature probed of 100 mK, but shows a macroscopic freezing below 200 mK. The magnetic moments have a very strong planar character. From the analysis of the magnetization curve within a mean-field model, the exchange couplings are found to be relatively weak and isotropic. At 1.5 K, the diffuse magnetic scattering is well reproduced by considering short-range correlations corresponding to Palmer-Chalker configurations. These results can be accounted for by a mean-field model which confirms that, with the $Er_2Sn_2O_7$ parameters deduced from the experiments, Palmer-Chalker configurations, stabilized by the dipolar interactions, should be the ground state. In that context, the absence of ordering in $Er_2Sn_2O_7$ remains an open issue, but the present estimation of the CEF parameters and exchange couplings appears to be a starting point for further theoretical calculation.

ACKNOWLEDGMENTS

We would like to acknowledge F. Damay and G. André for comments about the use of the Fullproff suite as well as M. Gingras, B. Canals, and M. Zhitomirsky for fruitful discussions. We thank C. Paulsen for allowing us to use his SQUID dilution magnetometers.

TABLE IV. CEF calculations for different B_{nm} parameters: The two first transitions $E_{1,2}$ along with the g-Landé factors $g_\perp$ and $g_\parallel$ are listed.

B_{20} (K)	B_{40} (K)	B_{43} (K)	B_{60} (K)	B_{63} (K)	B_{66} (K)	E_1 (meV)	E_2 (meV)	$g_\parallel$	$g_\perp$
656	3010	755	738	−653	990	5.08	7.64	0.054	7.53
700						5.03	7.70	0.125	7.57
600						5.15	7.56	0.034	7.47
	2710					5.47	8.59	1.065	7.81
	3310					4.77	6.92	1.405	7.09
		800				4.90	7.41	0.013	7.52
		700				5.30	7.91	0.10	7.53
			800			5.74	7.91	0.052	7.47
			700			4.70	7.48	0.16	7.57
				−600		4.93	7.18	0.98	7.28
				−700		5.24	8.14	0.84	7.68
					1100	5.38	8.64	0.22	7.64
					900	4.81	6.75	0.17	7.39

APPENDIX A: CRYSTAL FIELD

The CEF parameters are determined using the standard Hamiltonian

$$\mathcal{H}_{\mathrm{CEF}} = \sum_{m,n} B_{nm} O_{nm}.$$

The transition between levels give rise to dispersionless modes in elastic neutron scattering data. The positions and intensities of these modes are fitted in the present study. To illustrate the sensitivity of our determination, we present in Table IV the results of CEF calculations for different sets of B_{nm}. The g-Landé factors are determined by considering the projection of the magnetic moment operator in the subspace spanned by the ground doublet wave functions. The error bars on the g-Landé factors are estimated from these calculations. We provide the energies of the two first transitions (experimentally observed at $E_1 = 5.1 \pm 0.05$ and $E_2 = 7.6 \pm 0.05$ meV) as well as $g_\perp$ and $g_\parallel$.

APPENDIX B: DETAILS ABOUT THE ψ_2 BASIS VECTOR

The description of the possible magnetic structures in $Er_2Ti_2O_7$ and $Er_2Sn_2O_7$ XY antiferromagnets is based on the symmetry analysis performed in the Fd-$3m$ space group for a $\mathbf{k} = 0$ propagation vector. As explained in the main text, $Er_2Ti_2O_7$ undergoes a transition towards an antiferromagnetic Néel phase below $T_N = 1.2$ K.[10–12] This ordered phase has a noncollinear structure, in which the magnetic moments are perpendicular to the local $\langle 111 \rangle$ axes. This configuration corresponds to the ψ_2 basis vector of the Γ_5 irreducible representation.

To better figure out this peculiar configuration, a different approach can be followed,[17,18] considering a series of XY degenerate classical configurations where the magnetic moment at site i is defined in a local frame $(\vec{a}_i, \vec{b}_i, \vec{e}_i)$ given in Table V. Each magnetic moment points along $\vec{u}_i = \cos\phi \vec{a}_i + \sin\phi \vec{b}_i$,

TABLE V. $(\vec{a}_i,\vec{b}_i,\vec{e}_i)$ frame for the different sites of a tetrahedron.

Site	1	2	3	4
CEF axis $\vec{e}_i$	$(1,1,-1)$	$(-1,-1,-1)$	$(-1,1,1)$	$(1,-1,1)$
Position	$(\frac{1}{4},\frac{3}{4},0)$	$(0,\frac{1}{2},0)$	$(0,\frac{3}{4},\frac{1}{4})$	$(\frac{1}{4},\frac{1}{2},\frac{1}{4})$
$\vec{a}_i$	$(-2,1,-1)$	$(2,-1,-1)$	$(2,1,1)$	$(-2,-1,1)$
$\vec{b}_i$	$(0,1,1)$	$(0,-1,1)$	$(0,1,-1)$	$(0,-1,-1)$

where ϕ is a continuous parameter. $\vec{e}_i$ is the local CEF axis. With these notations, the six domains of the ψ_2 magnetic structure are obtained for $\phi = n\pi/3$, $n = 0,\ldots,5$, while the ψ_1 (Refs. 13 and 17, also called ψ_3 in Refs. 14 and 18) are generated for $\phi = \pi/6 + n\pi/3$, $n = 0,\ldots,5$.

These configurations are classically degenerate since for arbitrary ϕ, the classical energy given by $E_c = [4\mathcal{J}_a - 2(3\mathcal{J}_b + \mathcal{J}_c)]m^2$, where $(\mathcal{J}_a,\mathcal{J}_b,\mathcal{J}_c)$ are the bond exchange parameters defined in the main text, does not depend on ϕ. The studies published in Refs. 17 and 18 have shown further that the zero-point energy $E_o(\phi)$, calculated in the spin-wave approximation as a function of ϕ, breaks this degeneracy, exhibiting weak minima for the six ψ_2 domains. A particular ordered ground state is thus selected by this quantum order by disorder mechanism.

APPENDIX C: MEAN-FIELD MODEL

The present mean-field study follows the approach of Ref. 16; it is based on the following Hamiltonian for R moments $\vec{J}_i$ at site i:

$$\mathcal{H} = \mathcal{H}_{\rm CEF} + \sum_{\langle i,j\rangle} \vec{J}_i(\tilde{\mathcal{J}} + \tilde{\mathcal{J}}{\rm dip}_{i,j})\langle\vec{J}_j\rangle + g_J\mu_B\vec{H}\cdot\vec{J}_i.$$

In this expression, $\vec{H}$ is an applied magnetic field, $\tilde{\mathcal{J}}$ denotes the anisotropic exchange tensor, and $\tilde{\mathcal{J}}{\rm dip}_{i,j}$ is the dipolar interaction limited to the contribution of the nearest neighbors. Various conventions have been used to define this anisotropic exchange.[16–18,34] Here we assume an exchange tensor which is diagonal in the $(\vec{a},\vec{b},\vec{c})$ frame linked with a R-R bond. Considering for instance the pair of Er^{3+} ions at $\vec{r}_1 = (1/4,3/4,0)a$ and $\vec{r}_2 = (0,1/2,0)a$, where a is the cubic lattice constant, we define the local bond frame as $\vec{a}_{12} = (0,0,-1)$, $\vec{b}_{12} = 1/\sqrt{2}(1,-1,0)$, and $\vec{c}_{12} = 1/\sqrt{2}(-1,-1,0)$:

$$\vec{J}_i\tilde{\mathcal{J}}\vec{J}_j = \sum_{\mu,\nu=x,y,z} J_i^\mu\left(\mathcal{J}_a a_{ij}^\mu a_{ij}^\nu + \mathcal{J}_b b_{ij}^\mu b_{ij}^\nu + \mathcal{J}_c c_{ij}^\mu c_{ij}^\nu\right)J_j^\nu + \mathcal{J}_4\sqrt{2}\vec{b}_{ij}(\vec{J}_i\times\vec{J}_j).$$

Owing to the form of the dipolar interaction, we have

$$\tilde{\mathcal{J}}{\rm dip}_{i,j} = D_{\rm nn}(\vec{a}_{ij}\vec{a}_{ij} + \vec{b}_{ij}\vec{b}_{ij} - 2\vec{c}_{ij}\vec{c}_{ij}),$$

with $D_{\rm nn} = \frac{\mu_o}{4\pi}\frac{(g_J\mu_B)^2}{r_{\rm nn}^3}$ and where $r_{\rm nn}$ is the nearest neighbor distance in the pyrochlore lattice. If we incorporate it in the anisotropic exchange constants $(\mathcal{J}_a,\mathcal{J}_b,\mathcal{J}_c)$, we obtain

$$\mathcal{J}'_a = \mathcal{J}_a + D_{\rm nn},\quad \mathcal{J}'_b = \mathcal{J}_b + D_{\rm nn},\quad \mathcal{J}'_c = \mathcal{J}_c - 2D_{\rm nn}.$$

As usual in mean-field approximations, a self-consistent treatment is carried out to solve the problem: Starting from a random configuration for the $\langle\vec{J}_j\rangle$, the contribution to $\mathcal{H}$ at site i is diagonalized in the Hilbert space of the Er^{3+} magnetic moment defined by the $\{|J_z\rangle\}, J_z = -15/2,\ldots,15/2$ basis vectors, and taking into account the external magnetic field $\vec{H}$ as well as the molecular field $\sum_{\langle i,j\rangle}\vec{J}_i(\tilde{\mathcal{J}} + \tilde{\mathcal{J}}{\rm dip}_{i,j})\langle\vec{J}_j\rangle$. This yields the energies $E_{i,\mu}$ and the wave functions $|\psi_{i,\mu}\rangle$. The updated magnetic moments:

$$\langle\vec{J}_i\rangle = \sum_\mu \frac{e^{-E_{i,\mu}/k_BT}}{Z}\langle\psi_{i,\mu}|\vec{J}_i|\psi_{i,\mu}\rangle,$$
$$Z = \sum_\mu \exp(-E_{i,\mu}/k_BT)$$

is used to proceed at site j, and this is repeated until convergence. The magnetization is then given by

$$M(\vec{H}) = \sum_i \vec{m}_i\frac{\vec{H}}{H}.$$

APPENDIX D: RELATION WITH QUANTUM PSEUDOSPIN HALF MODELS

The anisotropic exchange Hamiltonian can be rewritten in terms of couplings between the spin components of a pseudospin half defined in the subspace of the ground CEF doublet:

$$\mathcal{H}' = \sum_{i,j} {\rm J}_{zz}{\rm S}_i^z{\rm S}_j^z - {\rm J}_\pm({\rm S}_i^+{\rm S}_j^- + {\rm S}_i^-{\rm S}_j^+) + {\rm J}_{\pm\pm}(\gamma_{ij}{\rm S}_i^+{\rm S}_j^+ + \gamma_{ij}^*{\rm S}_i^-{\rm S}_j^-) + {\rm J}_{z\pm}\left[{\rm S}_i^z(\zeta_{ij}{\rm S}_j^+ + \zeta_{ij}^*{\rm S}_j^-) + i\leftrightarrow j\right],$$

TABLE VI. Anisotropic exchange parameters for $Er_2Ti_2O_7$ and $Er_2Sn_2O_7$. $({\rm J}_{\pm\pm}, {\rm J}_\pm, {\rm J}_{z\pm}, {\rm J}_{zz})$ are given in 10^{-2} meV, while the other sets are in K. Positive values correspond to AF couplings.

Coupling	$Er_2Ti_2O_7$ (Ref. 17)	$Er_2Ti_2O_7$ (Ref. 36)	$Er_2Sn_2O_7$ (present work)
${\rm J}_{\pm\pm}$	4.2 (± 0.5)	3.2 (± 1)	7.4 (± 1.5)
${\rm J}_\pm$	6.5 (± 0.75)	6.7 (± 1)	1.35 (± 1.5)
${\rm J}_{z\pm}$	−0.88 (± 1.5)	1.32 (± 0.5)	0.025 (± 0.01)
${\rm J}_{zz}$	−2.5 (± 1.8)	−1.75 (± 0.4)	0.0
$\mathcal{J}'_a$	−0.056 (± 0.06)	−0.008 (± 0.01)	0.052 (± 0.017)
$\mathcal{J}'_b$	0.10 (± 0.01)	0.072 (± 0.005)	0.052 (± 0.005)
$\mathcal{J}'_c$	0.034 (± 0.07)	0.061 (± 0.01)	−0.004 (± 0.005)
$\mathcal{J}_4$	0.02 (± 0.03)	± 0.005	0
$\mathcal{J}_a$	−0.078 (± 0.06)	−0.03 (± 0.01)	0.03 (± 0.017)
$\mathcal{J}_b$	0.078 (± 0.01)	0.05 (± 0.005)	0.03 (± 0.005)
$\mathcal{J}_c$	0.078 (± 0.07)	0.105 (± 0.01)	0.04 (± 0.005)
$\mathcal{J}_4$	0.02 (± 0.03)	± 0.005	± 0.005
$g_\perp$	5.97	6.8	7.52
$g_\parallel$	2.45	2.6	0.054

$(\mathsf{J}_{\pm\pm},\mathsf{J}_{\pm},\mathsf{J}_{z\pm},\mathsf{J}_{zz})$ is the set of effective exchange parameters. Note that "sanserif" notations refer to local bases. The states of this pseudospin half span the ground CEF wave functions doublet, using the relation

$$g_J\vec{\mathsf{J}} = g\vec{\mathsf{S}} \quad \text{or} \quad \vec{\mathsf{J}} = \lambda\vec{\mathsf{S}}. \tag{D1}$$

In the context of pyrochlores, the $\lambda = \frac{g}{g_J}$ matrix is diagonal and takes the form

$$\lambda = \begin{pmatrix} \lambda_\perp & & \\ & \lambda_\perp & \\ & & \lambda_z \end{pmatrix}. \tag{D2}$$

We call M the matrix that connects the local and global bases and A the matrix connecting $(\mathsf{S_x},\mathsf{S_y},\mathsf{S_z})$ and $(\mathsf{S}_+,\mathsf{S}_-,\mathsf{S_z})$ (we omit the indexes for sake of clarity), so that

$$\vec{J} = M\lambda A\vec{\mathsf{S}}, \tag{D3}$$

$$A = \begin{pmatrix} 1/2 & 1/2 & \\ -i/2 & i/2 & \\ & & 1 \end{pmatrix}, \tag{D4}$$

with $\vec{\mathsf{S}} = (\mathsf{S}_+,\mathsf{S}_-,\mathsf{S_z})$. We thus have

$$\mathcal{H} = \sum_{ij,uv} \mathsf{S}_i^u \left(A^T\lambda M_i^T \mathcal{J} M_j \lambda A\right)^{uv} \mathsf{S}_i^v \tag{D5}$$

and we finally get the following relations:

$$\mathsf{J}_{zz} = \lambda_z^2 \frac{\mathcal{J}_a - 2\mathcal{J}_c - 4\mathcal{J}_4}{3},$$
$$\mathsf{J}_{\pm} = -\lambda_\perp^2 \frac{2\mathcal{J}_a - 3\mathcal{J}_b - \mathcal{J}_c + 4\mathcal{J}_4}{12},$$
$$\mathsf{J}_{z\pm} = \lambda_\perp\lambda_z \frac{\mathcal{J}_a + \mathcal{J}_c - \mathcal{J}_4}{3\sqrt{2}},$$
$$\mathsf{J}_{\pm\pm} = \lambda_\perp^2 \frac{2\mathcal{J}_a + 3\mathcal{J}_b - \mathcal{J}_c + 4\mathcal{J}_4}{12},$$

and conversely

$$\mathcal{J}_a = \frac{4}{3}\frac{\mathsf{J}_{\pm\pm} - \mathsf{J}_{\pm}}{\lambda_\perp^2} + \frac{4\sqrt{2}}{3}\frac{\mathsf{J}_{z\pm}}{\lambda_\perp\lambda_z} + \frac{1}{3}\frac{\mathsf{J}_{zz}}{\lambda_z^2},$$
$$\mathcal{J}_b = 2\frac{\mathsf{J}_{\pm\pm} + \mathsf{J}_{\pm}}{\lambda_\perp^2},$$
$$\mathcal{J}_c = \frac{2}{3}\frac{-\mathsf{J}_{\pm\pm} + \mathsf{J}_{\pm}}{\lambda_\perp^2} + \frac{4\sqrt{2}}{3}\frac{\mathsf{J}_{z\pm}}{\lambda_\perp\lambda_z} - \frac{2}{3}\frac{\mathsf{J}_{zz}}{\lambda_z^2},$$
$$\mathcal{J}_4 = \frac{2}{3}\frac{\mathsf{J}_{\pm\pm} - \mathsf{J}_{\pm}}{\lambda_\perp^2} - \frac{\sqrt{2}}{3}\frac{\mathsf{J}_{z\pm}}{\lambda_\perp\lambda_z} - \frac{1}{3}\frac{\mathsf{J}_{zz}}{\lambda_z^2}.$$

Table VI provides the different sets of anisotropic exchange parameters for $Er_2Ti_2O_7$ (Refs. 17 and 36) and $Er_2Sn_2O_7$ (present work) deduced from this transformation. This procedure is similar to the ones detailed in Refs. 17, 34, and 45.

[1] C. Lacroix, P. Mendels, and F. Mila, Eds., *Introduction to Frustrated Magnetism* (Springer, Berlin, 2011).

[2] J. Villain, R. Bidaux, J.-P. Carton, and R. Conte, J. Phys. **41**, 1263 (1980).

[3] J. S. Gardner, M. J. P. Gingras, and J. E. Greedan, Rev. Mod. Phys. **82**, 53 (2010).

[4] S. T. Bramwell and M. J. P. Gingras, Science **294**, 1495 (2001).

[5] J. M. D. Champion and P. C. W. Holdsworth, J. Phys.: Condens. Matter **16**, S665 (2004).

[6] P. Stasiak, P. A. McClarty, and M. J. P. Gingras, arXiv:1108.6053.

[7] K. Matsuhira, Y. Hinatsu, K. Tenya, H. Amitsuka, and T. Sakakibara, J. Phys. Soc. Jpn **71**, 1576 (2002).

[8] P. M. Sarte, H. J. Silverstein, B. T. K. Van Wyk, J. S. Gardner, Y. Qiu, H. D. Zhou, and C. R. Wiebe, J. Phys.: Condens. Matter **23**, 382201 (2011).

[9] J. Lago, T. Lancaster, S. J. Blundell, S. T. Bramwell, F. L. Pratt, M. Shirai, and C. Baines, J. Phys.: Condens. Matter **17**, 979 (2005).

[10] W. J. Blöte, R. F. Wielinga, and W. J. Huiskamp, Physica **43**, 549 (1969).

[11] M. J. Harris, S. T. Bramwell, T. Zeiske, D. F. McMorrow, and P. J. C. King, J. Magn. Magn. Mater. **177**, 757 (1998).

[12] R. Siddharthan, B. S. Shastry, A. P. Ramirez, A. Hayashi, R. J. Cava, and S. Rosenkranz, Phys. Rev. Lett. **83**, 1854 (1999).

[13] J. D. M. Champion, M. J. Harris, P. C. W. Holdsworth, A. S. Wills, G. Balakrishnan, S. T. Bramwell, E. Cizmar, T. Fennell, J. S. Gardner, J. Lago, D. F. McMorrow, M. Orendac, A. Orendacova, D. McK. Paul, R. I. Smith, M. T. F. Telling, and A. Wildes, Phys. Rev. B **68**, 020401(R) (2003).

[14] A. Poole, A. S. Wills, and E. Lelièvre-Berna, J. Phys.: Condens. Matter **19**, 452201 (2007).

[15] S. E. Palmer and J. T. Chalker, Phys. Rev. B **62**, 488 (2000); J. T. Chalker, P. C. W. Holdsworth, and E. F. Shender, Phys. Rev. Lett. **68**, 855 (1992).

[16] P. A. McClarty, S. H. Curnoe, and M. J. P. Gingras, J. Phys.: Conf. Ser. **145**, 012032 (2009).

[17] L. Savary, K. A. Ross, B. D. Gaulin, J. P. C. Ruff, and L. Balents, Phys. Rev. Lett. **109**, 167201 (2012).

[18] M. E. Zhitomirsky, M. V. Gvozdikova, P. C. W. Holdsworth, and R. Moessner, Phys. Rev. Lett. **109**, 077204 (2012).

[19] C. Paulsen, in *Introduction to Physical Techniques in Molecular Magnetism: Structural and Macroscopic Techniques - Yesa 1999*, edited by F. Palacio, E. Ressouche, and J. Schweizer (Servicio de Publicaciones de la Universidad de Zaragoza, Zaragoza, 2001), p. 1.

[20] On 4F2 we used a fixed final energy ($E_f = 5$ meV), yielding an instrumental resolution of about 0.25 meV. A nitrogen-cooled beryllium filter placed in the scattered beam to eliminate harmonics.

[21] P. Schiffer, A. P. Ramirez, D. A. Huse, P. L. Gammel, U. Yaron, D. J. Bishop, and A. J. Valentino, Phys. Rev. Lett. **74**, 2379 (1995).

[22] J. S. Gardner *et al.*, Phys. Rev. B **68**, 180401(R) (2003).

[23] N. Hamaguchi, T. Matsushita, N. Wada, Y. Yasui, and M. Sato, Phys. Rev. B **69**, 132413 (2004).

[24]E. Lhotel, C. Paulsen, P. D. de Réotier, A. Yaouanc, C. Marin, and S. Vanishri, Phys. Rev. B **86**, 020410(R) (2012).
[25]J. P. C. Ruff, J. P. Clancy, A. Bourque, M. A. White, M. Ramazanoglu, J. S. Gardner, Y. Qiu, J. R. D. Copley, M. B. Johnson, H. A. Dabkowska, and B. D. Gaulin, Phys. Rev. Lett. **101**, 147205 (2008).
[26]H. B. Cao, I. Mirebeau, A. Gukasov, P. Bonville, and C. Decorse, Phys. Rev. B **82**, 104431 (2010).
[27]S. S. Sosin, L. A. Prozorova, M. R. Lees, G. Balakrishnan, and O. A. Petrenko, Phys. Rev. B **82**, 094428 (2010).
[28]O. A. Petrenko, M. R. Lees, and G. Balakrishnan, J. Phys.: Condens. Matter **23**, 164218 (2011).
[29]H. Cao, A. Gukasov, I. Mirebeau, P. Bonville, C. Decorse, and G. Dhalenne, Phys. Rev. Lett. **103**, 056402 (2009).
[30]Y. Izyumov and V. E. Naish, J. Magn. Magn. Mater. **12**, 239 (1979); O. V. Kovalev, *Irreducible Representations of the Space Groups* (Gordon and Breach, New York, 1965).
[31]Here we adopt the notations of Refs. 13 and 17; note that they are different from those used in Refs. 14 and 18.
[32]J. Rodriguez-Carvajal, Physica B **192**, 55 (1993), http://www.ill.eu/sites/fullprof/
[33]The sample being a powder, the demagnetizing factor N is hard to estimate. However, the main characteristics of the exchange tensor deduced from the refinement of the magnetization curve are only slightly affected by the chosen value of N, so that the present analysis does not depend on its exact value.
[34]J. D. Thompson, P. A. McClarty, H. M. Ronnow, L. P. Regnault, A. Sorge, and M. J. P. Gingras, Phys. Rev. Lett. **106**, 187202 (2011)
[35]B. Z. Malkin, T. T. A. Lummen, P. H. M. van Loosdrecht, G. Dhalenne, and A. R. Zakirov, J. Phys.: Condens. Matter **22**, 276003 (2010).
[36]P. Bonville, S. Petit, I. Mirebeau, J. Robert, E. Lhotel, and C. Paulsen, J. Phys.: Condens. Matter **25**, 275601 (2013).
[37]Fits were performed setting $\mathcal{J}_4$ to a series of values between -0.02 and $+0.02$ (which is about 50% of the symmetric constants). For $\mathcal{J}_4$ larger than 0.01, the magnetization curve could not be reproduced. Note that, whatever $\mathcal{J}_4$, all the sets of parameters that reproduce the magnetization curve fall in the Palmer-Chalker part of the mean-field phase diagram of Fig. 5.
[38]L.-J. Chang, S. Onoda, Y. Su, Y.-J. Kao, K.-D. Tsuei, Y. Yasui, K. Kakurai, and M. R. Lees, Nat. Commun. **3**, 992 (2012).
[39]A. Yaouanc, P. Dalmas de Réotier, P. Bonville, J. A. Hodges, V. Glazkov, L. Keller, V. Sikolenko, M. Bartkowiak, A. Amato, C. Baines, P. J. C. King, P. C. M. Gubbens, and A. Forget, Phys. Rev. Lett. **110**, 127207 (2013).
[40]P. Bonville, J. A. Hodges, M. Ocio, J.-P. Sanchez, P. Vulliet, S. Sosin, and D. Braithwaite, J. Phys.: Condens. Matter **15**, 7777 (2003).
[41]A. S. Wills, M. E. Zhitomirsky, B. Canals, J. P. Sanchez, P. Bonville, P. Dalmas de Réotier and A. Yaouanc, J. Phys.: Condens. Matter **18**, L37 (2006).
[42]O. Cépas, A. P. Young, and B. S. Shastry, Phys. Rev. B **72**, 184408 (2005).
[43]J. R. Stewart, J. S. Gardner, Y. Qiu, and G. Ehlers, Phys. Rev. B **78**, 132410 (2008).
[44]A. G. Del Maestro and M. J. P. Gingras, J. Phys.: Condens. Matter **16**, 3339 (2004).
[45]S. H. Curnoe, Phys. Rev. B **78**, 094418 (2008); **75**, 212404 (2007).